Global Environmental Science
www.sciltp.com/journals/ges

Article

Evaluation of the Heterogeneous Fenton Activity of Ash Derived from Ferric-Salt-Conditioned Waste Activated Sludge

Yoon Ho Choi [1], Minjeong Kim [1], Changha Lee [2] and Min Sik Kim [1,*]

[1] Department of Climate, Environmental and Energy, Climate Technology Research Center, Jeonbuk National University, 567 Baekje-daero, Deokjin-gu, Jeonju-si 54896, Jeonbuk-do, Republic of Korea
[2] Department of Chemical and Biological Engineering, Institute of Chemical Process (ICP), Institute of Engineering Research, Seoul National University, Seoul 08826, Republic of Korea
* Correspondence: minsik@jbnu.ac.kr

How To Cite: Choi, Y.H.; Kim, M.; Lee, C.; et al. Evaluation of the Heterogeneous Fenton Activity of Ash Derived from Ferric-Salt-Conditioned Waste Activated Sludge. *Glob. Environ. Sci.* **2026**, *2*(4), 541–552. https://doi.org/10.53941/ges.2026.100033

Publication History

Received: 31 August 2026
Revised: 12 October 2026
Accepted: 4 November 2026
Published: 20 November 2026

Keywords

waste activated sludge ash;
adsorption;
heterogeneous Fenton catalyst;
iron leaching;
homogeneous Fenton reaction

Abstract: Waste activated sludge (WAS)-derived materials have been explored for organic pollutant removal through adsorption and heterogeneous Fenton oxidation. However, their heterogeneous Fenton activity remains uncertain because the contribution of dissolved Fe has not been adequately evaluated. In this study, Fe-containing WAS ash (FeSA) was prepared through Fe conditioning followed by dewatering, drying, and thermal treatment, mimicking a conventional WAS treatment process. Its adsorption and Fenton oxidation performances were evaluated using 4-chlorophenol (4-CP) and Reactive Black 5. FeSA exhibited adsorption capacities comparable to those of unconditioned WAS ash (SA) but substantially greater oxidative removal of both pollutants at pH 4, which decreased markedly at pH 5. At pH 4, up to ~20 μM Fe was dissolved, predominantly as Fe(III) from SA but as Fe(II) from FeSA. To assess the contribution of leached Fe(II), a homogeneous Fenton system containing 5 μM Fe(II), comparable to the level released from FeSA, was tested and achieved nearly complete oxidation of 0.1 mM 4-CP with a substantially higher stoichiometric efficiency of hydrogen peroxide utilization (6.86%) than FeSA and the reference Fe solids (≤2.02%). These findings highlight the substantial contribution of micromolar dissolved Fe(II) to Fenton oxidation and suggest that FeSA may be better viewed as a multifunctional material combining pollutant adsorption with the release of catalytically active Fe(II) for homogeneous Fenton oxidation, rather than as a conventional heterogeneous Fenton catalyst.

Highlights

- Ferric conditioning improves WAS dewaterability and enables its valorization as a Fenton catalyst.
- FeSA exhibits oxidative removal of pollutants under acidic conditions in the presence of H_2O_2.
- FeSA releases Fe in its reduced form, which contributes to homogeneous Fenton oxidation.

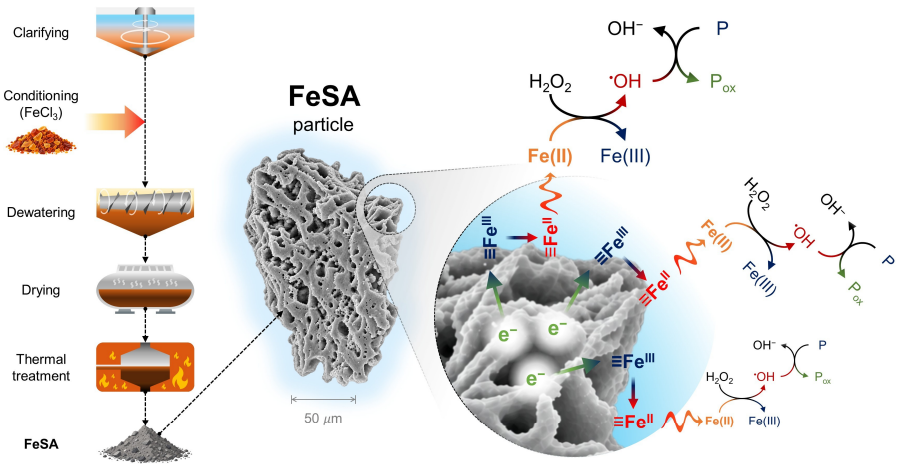

Copyright: © 2026 by the authors. This is an open access article under the terms and conditions of the Creative Commons Attribution (CC BY) license (https://creativecommons.org/licenses/by/4.0/).
Publisher's Note: Scilight stays neutral with regard to jurisdictional claims in published maps and institutional affiliations.

1. Introduction

The treatment of municipal wastewater has long relied on the activated sludge process, in which microbial communities remove organic matter and nutrients. Waste activated sludge (WAS) is inevitably generated during this process, necessitating a series of subsequent treatment steps prior to its final disposal or beneficial reuse. A representative WAS-handling sequence in wastewater treatment plants without anaerobic digestion includes thickening, chemical conditioning, mechanical dewatering, drying, thermal treatment, and final disposal (Figure 1a) [1–3]. Because WAS contains a large amount of water retained within microbial cells, extracellular polymeric substances, and WAS floc matrices, it exhibits poor dewaterability, making WAS handling a major contributor to the operating cost of wastewater treatment plants (WWTPs) [4–7]. To improve the dewaterability of thickened WAS withdrawn from secondary clarifiers, chemical conditioning is commonly applied prior to mechanical dewatering. Although organic polymer flocculants are widely used for WAS conditioning, inorganic coagulants, particularly ferric chloride ($FeCl_3$), can also be employed because their hydrolysis products serve as skeletal builders, promoting the formation of compact and mechanically robust WAS flocs that are advantageous for high-pressure dewatering [8,9]. Ferric hydroxide precipitates formed during Fe conditioning remain associated with the dewatered WAS solids throughout subsequent thermal treatment.

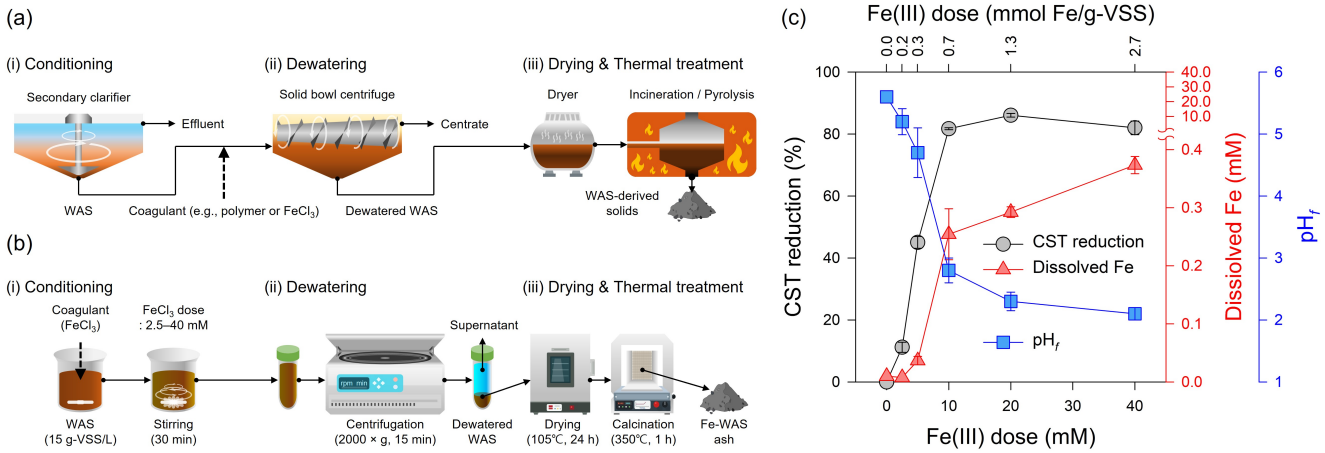

Figure 1. Overview of Fe-assisted WAS treatment and FeSA production. (**a**) Schematic diagram of the conventional WAS treatment train. (**b**) Laboratory-scale procedure for preparing FeSA designed to mimic the conventional treatment train. (**c**) Effects of Fe(III) dose on the CST reduction of WAS and on the dissolved Fe concentration and final pH_f of the WAS filtrate.

As increasing amounts of WAS are generated at WWTPs, the valorization of thermally derived WAS residues, including ashes produced by incineration and chars produced by pyrolysis, has attracted considerable attention. Such materials have been widely investigated as adsorbents for pollutant removal because their porous structures and surface functionalities can provide effective sorption sites [10–12]. Beyond their conventional use as adsorbents, Fe-containing thermally derived WAS materials have also been investigated as bifunctional materials capable of not only adsorbing pollutants but also promoting their oxidative degradation through heterogeneous Fenton-like reactions in the presence of hydrogen peroxide (H_2O_2) [13–18]. Most previous studies have focused on WAS-derived chars prepared by pyrolysis under N_2 conditions [13–17], whereas only a single study has examined a calcined WAS-derived material prepared by thermal treatment under air conditions [18]. Despite differences in their preparation methods, these studies generally attributed the removal of organic pollutants (primarily dyes) to heterogeneous Fenton-like reactions. This interpretation was supported, to varying extents, by the enhanced degradation observed after H_2O_2 addition following adsorption equilibration, substantial total organic carbon removal, retained catalytic activity over repeated cycles, spectroscopic detection of hydroxyl radicals (•OH), and measurements showing relatively low Fe leaching compared with the total Fe incorporated in the catalysts.

From a mechanistic perspective, distinguishing heterogeneous and homogeneous Fenton pathways is essential for determining whether these materials function as true heterogeneous catalysts or merely as iron reservoirs that release dissolved Fe species capable of activating H_2O_2 [19–21]. Previous studies on Fe-containing WAS-derived materials have not always clearly distinguished these two pathways. Although the reported dissolved Fe concentrations were relatively low, they still reached the micromolar range (3.8–11.8 μM at pH 4 [13,15,16,18]) and thus may not be negligible in systems containing millimolar concentrations of H_2O_2 (7.4–39 mM [13–18]). The potential contribution of dissolved Fe to Fenton oxidation may have been underestimated, partly because of its low concentration relative to the total Fe content of the solid materials. Moreover, the temporal evolution and oxidation states of

 https://doi.org/10.53941/ges.2026.100033

dissolved Fe during the reactions were rarely investigated. Accordingly, it remains insufficiently resolved whether the reported oxidation activity is attributable primarily to heterogeneous surface reactions or is partially mediated by dissolved Fe species.

Meanwhile, most WAS-derived heterogeneous Fenton catalysts reported in previous studies were purposefully fabricated through additional processing of dewatered WAS or WAS-derived chars, including chemical activation, Fe impregnation, and controlled thermal treatment, rather than being obtained directly from conventional WAS-handling operations [13–18]. Although such post-processing may enhance catalytic performance, the additional use of chemicals, energy, and processing steps may limit the practical applicability of these approaches from the perspective of waste valorization and routine WAS management. To date, the potential of Fe-containing WAS residues generated through Fe conditioning, dewatering, and subsequent thermal treatment to function as heterogeneous Fenton catalysts has not been systematically investigated.

To address these gaps, Fe-containing WAS-derived ash (denoted as FeSA) was prepared through a laboratory-scale simulation of a representative WAS-handling sequence (Figure 1b). The pollutant removal performance of FeSA prepared with different ferric coagulant dosages was evaluated in two sequential stages consisting of initial adsorption followed by H_2O_2-assisted oxidation at pH 4 and 5 using 4-chlorophenol (4-CP) as a representative recalcitrant organic compound and Reactive Black 5 (RB5) as a model azo dye. Temporal profiles of dissolved Fe, including Fe(II) and total dissolved Fe, were monitored in the absence of H_2O_2. Based on the measured dissolved Fe concentrations, corresponding homogeneous and heterogeneous Fenton systems were comparatively evaluated by monitoring 4-CP degradation and H_2O_2 decomposition. This study provides a critical assessment of whether FeSA functions as a true heterogeneous Fenton catalyst or merely as an iron reservoir and establishes a practical framework for evaluating waste-derived materials as heterogeneous Fenton catalysts.

2. Materials and Methods

2.1. Materials

WAS sample was collected from the sludge withdrawal line of the secondary clarifier at a full-scale WWTP located in Jeonju-si, Republic of Korea. The collected WAS was gravity-thickened to a volatile suspended solids (VSS) concentration of approximately 16.5 g-VSS/L and stored at 4 °C until use. All chemicals were of reagent grade and used without further purification. The following chemicals were obtained from Sigma-Aldrich: copper(II) sulfate pentahydrate ($CuSO_4·5H_2O$), iron(II) sulfate heptahydrate ($FeSO_4·7H_2O$), iron(III) chloride hexahydrate ($FeCl_3·6H_2O$), iron(III) oxide (Fe_2O_3), goethite (α-FeOOH), 4-CP, RB5, sodium hydroxide (NaOH), 2,9-dimethyl-1,10-phenanthroline (DMP), 1,10-phenanthroline, titanium(IV) oxysulfate solution, H_2O_2 solution (30 wt%), *tert*-butanol (*t*-BuOH), phosphoric acid (H_3PO_4; ≥85 wt%), nitric acid (HNO_3, 70%), and perchloric acid ($HClO_4$, 70%). High-performance liquid chromatography (HPLC) grade methanol (J.T. Baker) was used as the HPLC mobile phase. All solutions were prepared using deionized (DI) water (≥18.2 MΩ cm).

2.2. Preparation of FeSA

FeSA was prepared by simulating the representative WAS-handling sequence illustrated in Figure 1b. Thickened WAS (180 mL; 16.5 g-VSS/L) was mixed with 20 mL of an $FeCl_3$ stock solution, resulting in a total volume of 200 mL and a final VSS concentration of approximately 15 g-VSS/L. The concentrations of the $FeCl_3$ stock solutions were varied from 25 to 400 mM to obtain final Fe(III) concentrations of 2.5–40 mM, corresponding to 0.17–2.67 mmol Fe/g-VSS. Immediately after the addition of the $FeCl_3$ solution, the suspension was rapidly mixed for 30 s and then gently stirred for 30 min. The Fe-conditioned WAS was centrifuged at 2000× *g* for 15 min, after which the supernatant was discarded and the resulting sludge cake was collected. The solids were transferred to alumina crucibles, dried at 110 °C for 5 h, and subsequently incinerated at 350 °C for 1 h in ambient air. The resulting ash was finely ground using an alumina mortar, thoroughly washed with DI water, oven-dried at 105 °C, and stored in a desiccator until use. The Fe-containing WAS-derived ash samples were designated according to the final Fe(III) concentration used for conditioning (e.g., FeSA20 for 20 mM $FeCl_3$). The ash prepared without $FeCl_3$ addition was designated as SA.

2.3. Characterization of FeSA

The morphology of FeSA was characterized using field-emission scanning electron microscopy (FE-SEM; S-4800, Hitachi, Tokyo, Japan) operated at an accelerating voltage of 15 kV. Prior to observation, the samples were coated with a thin platinum layer using a sputter coater (MC1000, Hitachi, Tokyo, Japan). The elemental composition and spatial distribution of elements were examined by energy-dispersive X-ray spectroscopy (EDS) coupled with the FE-SEM system. The specific surface area and average pore diameter were determined using a BET surface-area analyzer (BELSORP-mini X, MicrotracBEL, Osaka, Japan); the samples were degassed under N_2 at 200 °C for 8 h. Surface functional groups were analyzed using Fourier transform infrared spectroscopy (FTIR; FT/IR-8X, JASCO, Tokyo, Japan) equipped with a germanium attenuated total reflectance accessory over the spectral range of 400–4000 cm^{-1} at a resolution of 4 cm^{-1}. The crystalline phases of the samples were characterized by X-

ray diffraction (XRD; SmartLab, Rigaku, Tokyo, Japan) using Cu Kα radiation (λ = 1.5406 Å). The X-ray tube was operated at 45 kV and 200 mA. Diffraction patterns were collected over a 2θ range of 10–70° at a scanning rate of 5° min^{-1}. The obtained diffraction patterns were analyzed using HighScore Plus software (version 2.0, PANalytical). The surface chemical composition and chemical states were analyzed using X-ray photoelectron spectroscopy (XPS; Nexsa G2, Thermo Fisher Scientific, Waltham, MA, USA) equipped with a monochromatic Al Kα X-ray source (1486.6 eV). High-resolution spectra were deconvoluted by multi-peak fitting using Avantage software (version 6.6, Thermo Fisher Scientific).

2.4. Batch Experimental Procedure

All experiments were conducted in 150 mL conical beakers containing 100 mL of reaction solution under continuous magnetic stirring at room temperature (20 ± 2 °C). Reaction solutions were prepared by adding an aliquot of the target pollutant stock solution (4-CP or RB5) to DI water to obtain an initial concentration of 0.1 mM. The initial pH was adjusted to 4 or 5 using 0.1 M $HClO_4$, and no buffer was used to avoid possible interactions with FeSA, such as enhanced Fe dissolution. The reaction pH changed only slightly during the experiments and was maintained at the target value by adding 0.1 M $HClO_4$ or 0.1 M NaOH when necessary. Unless otherwise specified, H_2O_2 was added to obtain an initial concentration of 10 mM before the addition of FeSA. The reaction was initiated by adding 0.1 g of FeSA to the solution. For experiments designed to separately evaluate adsorption and oxidation, H_2O_2 was introduced after adsorption equilibrium had been reached (60 min). At predetermined intervals, 1-mL aliquots were withdrawn, filtered through 0.2 μm syringe filters, and immediately mixed with 20 μL of 1 M *t*-BuOH to quench further oxidation prior to the analysis of target pollutants, dissolved Fe species, or H_2O_2. All experiments were performed in triplicate, and data are presented as the mean ± standard deviation.

2.5. Analytical Methods

The dewaterability of the WAS samples before and after Fe conditioning was evaluated using a capillary suction time (CST) apparatus (Type 304B, Triton, Great Dunmow, UK). The improvement in dewaterability was expressed as the CST reduction (%), calculated as $(1 - CST_f/CST_i) \times 100$, where CST_i and CST_f denote the CST values before and after Fe conditioning, respectively. The concentrations of dissolved Fe, Cu(I), and H_2O_2 were determined using the 1,10-phenanthroline, DMP, and titanium sulfate colorimetric methods, respectively, with a UV-Vis spectrometer (Lambda 465, PerkinElmer, Shelton, CT, USA) [22–24]. Specifically, a 5-cm path-length quartz cuvette was used for the determination of micromolar Fe concentrations. RB5 decolorization was monitored by measuring the absorbance at 597 nm using the UV-Vis spectrometer. The concentration of 4-CP was determined using an HPLC (Ultimate 3000, Dionex, Sunnyvale, CA, USA) equipped with a UV-Vis detector (VWD-3400RS). Chromatographic separation was performed on an Acclaim™ C18 column (2.1 mm × 150 mm, 5 μm, 120 Å; Thermo Fisher Scientific) using a binary mobile phase consisting of methanol and 0.1% H_3PO_4 (35:65, *v*/*v*) at a flow rate of 0.8 mL/min.

3. Results and Discussion

3.1. Optimization of Fe Conditioning for FeSA Preparation

The thickened WAS exhibited an initial CST of 108.7 ± 3.0 s. To determine the appropriate Fe(III) dose for improving WAS dewaterability, $FeCl_3$ was added to thickened WAS at Fe(III) doses of 2.5–40 mM, followed by rapid mixing and gentle agitation for 30 min. Figure 1c summarizes the resulting CST reduction together with the dissolved Fe concentration in the filtrate ($[Fe]_{diss}$) and the final pH (pH_f) after conditioning. Increasing the Fe(III) dose from 2.5 to 10 mM significantly improved WAS dewaterability, as indicated by the increase in CST reduction from 11.2 to 81.7%. Beyond 10 mM, however, additional Fe(III) dosing produced only marginal improvements, with CST reduction reaching a maximum of 86.1% at 20 mM and then slightly decreasing to 82.0% at 40 mM. This maximum approached an estimated upper limit of approximately 91%, based on a CST of about 10 s for particle-free water. The $[Fe]_{diss}$ continued to increase with increasing Fe(III) dose. Despite this increase, the absolute $[Fe]_{diss}$ values remained very low relative to the applied Fe(III) dose. The ratio of $[Fe]_{diss}$ to the applied Fe(III) dose reached a maximum of only 2.61% at an Fe(III) dose of 20 mM, suggesting that the vast majority of the added Fe was retained in the WAS solids. Collectively, these results indicate that an Fe(III) dose of 10–20 mM (0.7–1.3 mmol Fe(III)/g-VSS) represents the optimal conditioning range for improving WAS dewaterability. This dosage range is consistent with a previous report, in which the optimum Fe(III) dose for WAS conditioning was approximately 0.31–1.30 mmol Fe(III)/g-dry solids [12].

3.2. Physicochemical Characterization of FeSA

Figure 2a shows a representative SEM image of FeSA20. Examination of four independently acquired SEM images revealed that FeSA20 consisted predominantly of irregularly shaped agglomerates with rough and porous surfaces and characteristic particle sizes of approximately 50–60 μm (Figure S1). A higher-magnification view of the selected region further revealed numerous surface cavities, protrusions, and irregular surface features (Figure S2). The corresponding BET surface area, total pore volume, and average pore diameter were 47.7 m^2/g, 0.09 cm^3/g, and 7.42 nm, respectively.

 https://doi.org/10.53941/ges.2026.100033

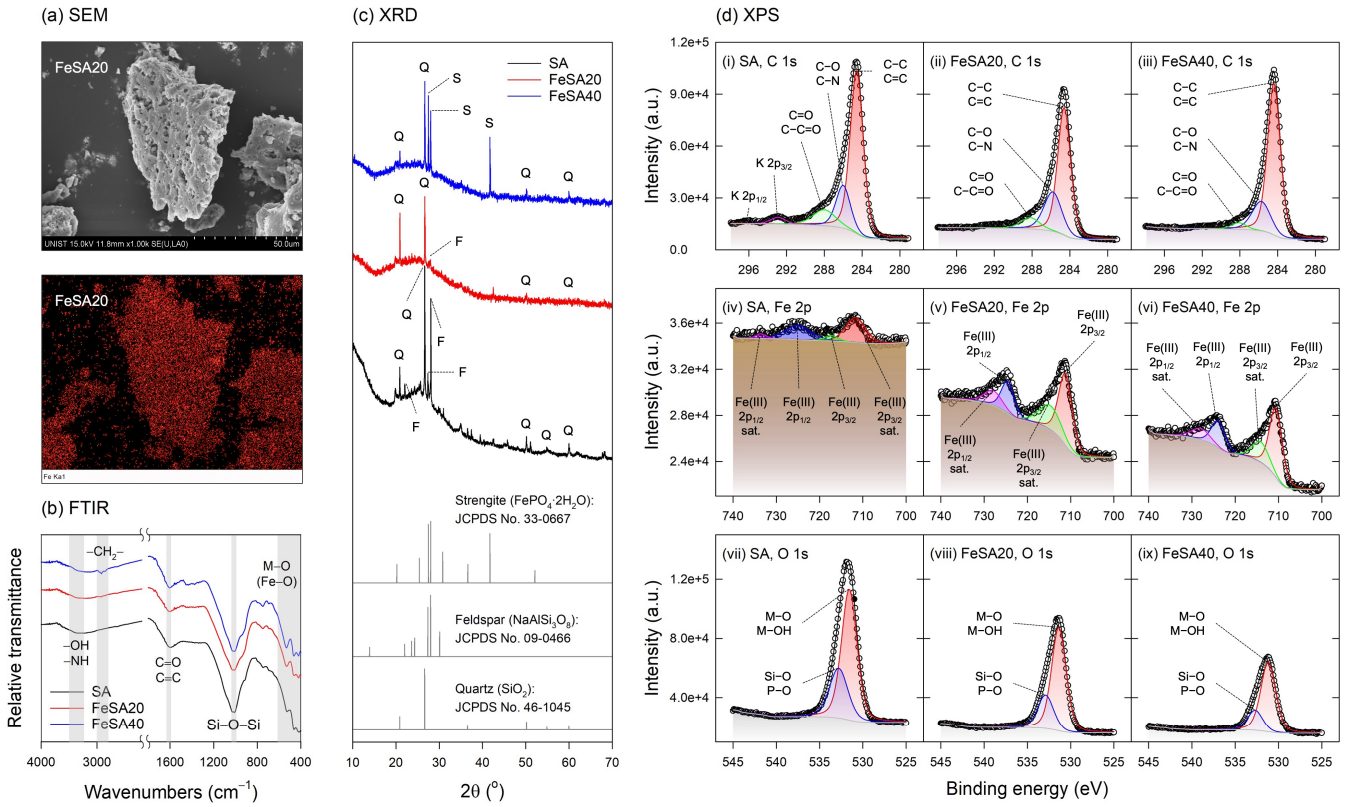

Figure 2. Physicochemical characterization of SA and FeSA materials. (**a**) Representative SEM image and corresponding EDS Fe elemental map of FeSA20. (**b**) FTIR spectra. (**c**) XRD patterns with reference diffraction patterns. (**d**) High-resolution XPS spectra of the C 1s, Fe 2p, and O 1s regions.

Fe elemental mapping by EDS showed that Fe was uniformly distributed throughout the FeSA20 particles rather than being confined to isolated regions (Figure 2a). This spatial distribution indicates that Fe introduced during WAS conditioning remained associated with the WAS-derived solid matrix after thermal treatment. EDS point analyses at three different locations on the FeSA20 surface yielded an average Fe content of 20.4 ± 2.7 wt% (Figure S3). This value was in good agreement with the bulk Fe content of 17.6 ± 0.2 wt%, determined by HNO_3 extraction of FeSA20 powder.

The FTIR spectra of SA, FeSA20, and FeSA40 exhibited similar absorption profiles, indicating that Fe conditioning did not substantially alter the overall surface functional group composition of the ash (Figure 2b). Broad absorption bands at 3200–3600 cm^{-1} were assigned to surface O–H and N–H stretching vibrations, whereas the band near 1600 cm^{-1} was attributed to overlapping contributions from aromatic C=C and C=O vibrations. The characteristic bands at approximately 1000 and 500 cm^{-1} corresponded to Si–O–Si and metal-oxygen vibrations, respectively.

The XRD patterns indicate that both SA and FeSA were predominantly amorphous, as evidenced by the broad diffuse halo centered over the 2θ range of 20–35° (Figure 2c). Superimposed on this amorphous background, the SA sample exhibited distinct diffraction peaks corresponding to quartz and alkali feldspar, representing the major residual crystalline phases of the ash matrix. These observations are consistent with the FTIR spectra (Figure 2b), which showed characteristic Si–O–Si vibrations while providing no evidence for substantial changes in the silicate framework after Fe conditioning. Following Fe conditioning, the amorphous character became more pronounced, accompanied by a marked reduction in quartz diffraction intensity and the virtual disappearance of the feldspar reflections. Meanwhile, weak diffraction peaks tentatively assigned to strengite ($FePO_4 \cdot 2H_2O$) emerged in FeSA20 and became more distinct in FeSA40, suggesting the progressive formation of Fe phosphate phases with increasing Fe dosage. The emergence of these diffraction peaks is likely attributable to the reaction between the introduced Fe(III) and phosphate species inherently present in the WAS matrix. The reduction in feldspar crystallinity may be attributed to partial acid-promoted dissolution during Fe(III) conditioning, as the hydrolysis of $FeCl_3$ lowers the WAS pH.

The surface chemical composition and chemical states of SA, FeSA20, and FeSA40 were further investigated by XPS, and high-resolution spectra of the major elements C, Fe, and O are presented in Figure 2d. The C 1s spectra exhibited similar peak distributions for all samples, with the dominant peak at approximately 284.5 eV assigned to C–C/C=C bonds, accompanied by smaller contributions from C–O/C–N and C=O/C–C=O species (Figure 2d(i–iii)). No

appreciable shifts in binding energy or the emergence of new carbon species were observed after Fe conditioning, indicating that the overall carbonaceous surface chemistry remained largely unchanged. In contrast, the Fe 2p spectra exhibited increased Fe signals after Fe conditioning, supporting Fe incorporation onto the WAS-derived ash surface (Figure 2d(iv–vi)). The Fe $2p_{3/2}$ peak centered at approximately 711.9 eV, together with the satellite feature near 730.1 eV, indicates that Fe(III) remained the predominant oxidation state in all samples. A weak component centered at approximately 715.7 eV may reflect a minor contribution from partially reduced Fe species formed during calcination in the presence of residual organic matter. Despite the increased Fe signal, the binding energies and spectral profiles remained essentially unchanged, indicating that Fe conditioning increased the amount of surface Fe while largely preserving its chemical state. Likewise, the O 1s spectra exhibited similar spectral profiles and binding energies for all samples (Figure 2d(vii–ix)). The lower-binding-energy component (~531 eV) was assigned to metal–oxygen/hydroxyl species, whereas the higher-binding-energy component (~533 eV) was attributed to Si–O/P–O species. The absence of appreciable peak shifts following Fe conditioning suggests that the overall oxygen coordination environment remained largely unchanged despite the incorporation of additional Fe.

3.3. Pollutant Removal Performance of FeSA

To evaluate the pollutant removal performance of FeSA, two representative organic pollutants with distinct chemical characteristics were selected: 4-CP as a model phenolic compound and RB5 as a model azo dye. The experiments were conducted at pH 4 and 5 to examine pollutant removal under conditions with different Fe solubilities. The temporal concentration profiles of the target pollutants during the sequential adsorption and oxidation processes are presented in Figure 3. For each pollutant and pH condition, the upper and lower panels show the normalized concentration (C/C_0) and its logarithmic transformation ($\ln(C/C_0)$), respectively. The initial 60 min represents the adsorption stage, after which H_2O_2 was added to initiate oxidation. The insets in the lower panels show enlarged views of the fitted regression lines for the 60–120 min time interval.

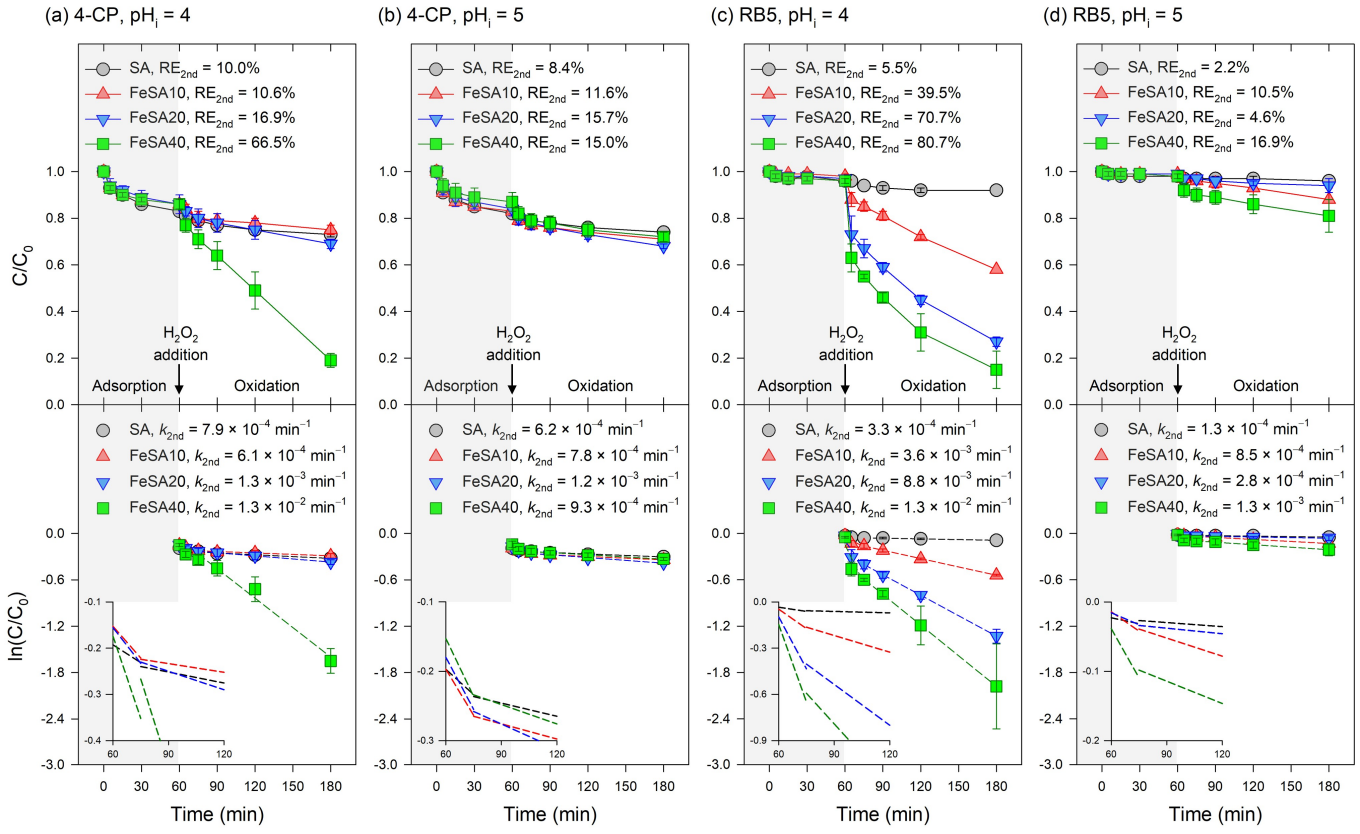

Figure 3. Time-dependent removal of target pollutants by SA, FeSA10, FeSA20, and FeSA40: (**a**) 4-CP at pH$_i$ = 4, (**b**) 4-CP at pH$_i$ = 5, (**c**) RB5 at pH$_i$ = 4, and (**d**) RB5 at pH$_i$ = 5. The initial 60 min corresponds to the adsorption stage, followed by the addition of H_2O_2 to initiate the oxidation stage. The lower panels show the corresponding pseudo-first-order kinetic plots for the oxidation stage, and the insets show enlarged views of the fitted regression lines over the 60–120 min interval. Reaction conditions: $[4\text{-CP}]_0 = [RB5]_0 = 0.1$ mM, $[H_2O_2]_0 = 10$ mM, and solid concentration = 1 g/L.

During the initial 60 min adsorption stage at pH 4, the control SA exhibited a 4-CP adsorption efficiency of 17.5 ± 1.0% (Figure 3a). The Fe-loaded SAs (FeSA10–FeSA40) showed comparable adsorption efficiencies

 https://doi.org/10.53941/ges.2026.100033

ranging from 13.8 to 14.3%. A similar trend was observed at pH 5, where the adsorption efficiencies of all materials ranged from 13.3 to 17.5% (Figure 3b). These results indicate that Fe loading and solution pH (4–5) had no significant effect on 4-CP adsorption.

Following H_2O_2 addition (after 60 min) at pH 4, a characteristic two-stage oxidation profile was observed for all materials (Figure 3a), consisting of an initial rapid oxidation phase during the first sampling interval (60–65 min), followed by a slower degradation stage. The two kinetic stages were identified based on independent pseudo-first-order regressions of the $\ln(C/C_0)$ plots, with excellent linearity ($R^2 \geq 0.98$) obtained for all tested conditions. Such a two-stage oxidation profile has frequently been reported during the degradation of organic compounds by homogeneous Fenton systems, in which an initial rapid oxidation stage is driven by the rapid generation of hydroxyl radicals (•OH) through the reaction of H_2O_2 with pre-existing Fe(II) (reaction 1), followed by a slower oxidation stage governed by the relatively slow regeneration of Fe(II) from Fe(III) (reaction 2) [25–27].

$$\mathrm{Fe(II) + H_2O_2 \rightarrow Fe(III) + {\cdot}OH + OH^- \ (k_1 = 63\ M^{-1}\ s^{-1})} \quad (1)$$

$$\mathrm{Fe(III) + H_2O_2 \rightarrow Fe(II) + HO_2^{\cdot} + H^+ \ (k_2 \leq 3 \times 10^{-3}\ M^{-1}\ s^{-1})} \quad (2)$$

Despite the similar two-stage kinetic behavior, the overall oxidation performance differed significantly among the materials. The oxidation removal efficiency during the second oxidation stage after excluding the contribution of adsorption (defined as RE2nd) remained low for SA (10.0%), FeSA10 (10.6%), and FeSA20 (16.9%), whereas FeSA40 achieved a considerably higher RE2nd of 66.5%. Consistent with the RE2nd values, the apparent pseudo-first-order rate constant for the slower oxidation phase (k2nd) showed a threshold-like increase with increasing Fe loading, following the order SA (7.9×10^{-4} min^{-1}) ≈ FeSA10 (6.1×10^{-4} min^{-1}) < FeSA20 (1.3×10^{-3} min^{-1}) ≪ FeSA40 (1.3×10^{-2} min^{-1}). Increasing the solution pH from 4 to 5 exerted little influence on the oxidation performance of SA, FeSA10, and FeSA20, whereas the superior oxidation performance of FeSA40 at pH 4 was markedly diminished at pH 5 (Figure 3b). Specifically, the RE2nd of FeSA40 decreased from 66.5 to 15.0%, accompanied by a decrease in k2nd from 1.3×10^{-2} to 9.3×10^{-4} min^{-1}.

In contrast to 4-CP, RB5 exhibited only limited adsorption onto SA, with an adsorption efficiency of 3.3 ± 0.4% at pH 4 (Figure 3c). The FeSA materials likewise exhibited low adsorption efficiencies (2.1–4.5%). The markedly lower adsorption of RB5 compared with 4-CP may be attributed to differences in their molecular properties. RB5 contains four sulfonate groups and is therefore strongly negatively charged in aqueous solution, which may result in electrostatic repulsion between RB5 and negatively charged sites on the WAS-derived ash surface [28,29]. In contrast, 4-CP, with a pK_a value of 9.38 [30], is predominantly present in its neutral form at pH 4. Its comparatively greater hydrophobicity and weaker electrostatic repulsion may therefore partly account for its higher adsorption onto the ash surface compared with RB5. A similarly negligible extent of RB5 adsorption was observed at pH 5, with adsorption efficiencies ranging from 1.3 to 2.3% for all materials (Figure 3d).

Upon H_2O_2 addition, FeSA10–FeSA40 exhibited a clear two-stage oxidation profile for RB5 at pH 4 (Figure 3c). Compared with 4-CP, RB5 underwent much greater oxidation during both the initial rapid and subsequent slower degradation phases. This higher oxidation efficiency of RB5 is likely driven by the intrinsically high reactivity of azo dyes toward •OH. While the second-order rate constant of RB5 with •OH has not been experimentally reported, the rate constants reported for azo dyes generally fall within the range of ~1–3 × 10^{10} M^{-1} s^{-1} [31], which is approximately 1.3–3.9 times higher than that of 4-CP (7.6 × 10^9 M^{-1} s^{-1} [32]). The initial oxidative degradation efficiencies (RE1st) of RB5 were 1.3, 10.0, 24.0, and 32.2% for SA, FeSA10, FeSA20, and FeSA40, respectively. The corresponding RE2nd values increased from 5.5% for SA to 39.5, 70.7, and 80.7%, respectively. Likewise, the k2nd values increased progressively with Fe loading, from 3.3 × 10^{-4} to 1.3 × 10^{-2} min^{-1}. However, at pH 5, the oxidative performance toward RB5 was markedly reduced for all materials (Figure 3d), as was the case for 4-CP, with RE2nd values remaining below 20% and the corresponding k2nd being approximately one order of magnitude lower than that at pH 4 (1.3×10^{-3} vs. 1.3×10^{-2} min^{-1}).

Based on the oxidation behaviors observed for both 4-CP and RB5 (Figure 3), we hypothesize that the oxidative degradation of these organic compounds in the FeSA/H_2O_2 system may have proceeded predominantly via dissolved Fe-mediated homogeneous Fenton reactions. Evidence supporting this hypothesis is the characteristic two-stage oxidation profile consistently observed for both pollutants at both pH values. As mentioned above, homogeneous Fenton reactions typically exhibit an initial rapid oxidation stage and a subsequent slower oxidation stage [25,26], whereas heterogeneous Fenton systems often exhibit a more gradual single-stage pseudo-first-order oxidation profile [33,34]. During the preceding 60 min adsorption stage, Fe species may be released from the FeSA, thereby accounting for the observed two-stage oxidation profile. This interpretation is further supported by the pronounced deterioration in oxidation performance with increasing pH from 4 to 5, particularly for FeSA40, because the sharp decrease in Fe(III) solubility over this critical pH window substantially limits the availability of dissolved Fe species [35,36].

3.4. Iron Leaching Behavior of SA and FeSA

To examine the above hypothesis (i.e., pollutant degradation proceeded predominantly via homogeneous

Fenton reactions driven by dissolved Fe species), the temporal evolution of dissolved Fe was monitored by separately quantifying Fe(II) and total dissolved Fe concentrations for SA, FeSA20, and FeSA40 at a constant pH 4 (Figure 4). In the SA suspension, the total dissolved Fe concentration increased rapidly during the initial stage, reaching 11.3 ± 1.6 μM at 60 min, and subsequently remained nearly constant throughout the remainder of the experiment (10.5 ± 3.5 μM at 240 min; Figure 4a). In contrast, FeSA exhibited a more gradual and sustained release of Fe. The total dissolved Fe concentrations in FeSA20 and FeSA40 reached 10.5 ± 1.1 and 21.6 ± 5.7 μM, respectively, at 240 min (Figure 4b,c). The contrasting Fe-release profiles may reflect differences in the solid-phase association of Fe between SA and FeSA. The rapid Fe release from SA might be associated with poorly crystalline or amorphous Fe species, which are generally more susceptible to dissolution than well-crystallized Fe phases [37,38]. Consistent with this possibility, no distinct crystalline Fe-containing phase was identified in SA (Figure 2c). In contrast, Fe conditioning resulted in the emergence of an Fe phosphate phase tentatively assigned to strengite, which became more apparent with increasing Fe dosage. Meanwhile, the greater extent of Fe release from FeSA, particularly FeSA40, is consistent with the higher Fe content of the Fe-conditioned materials.

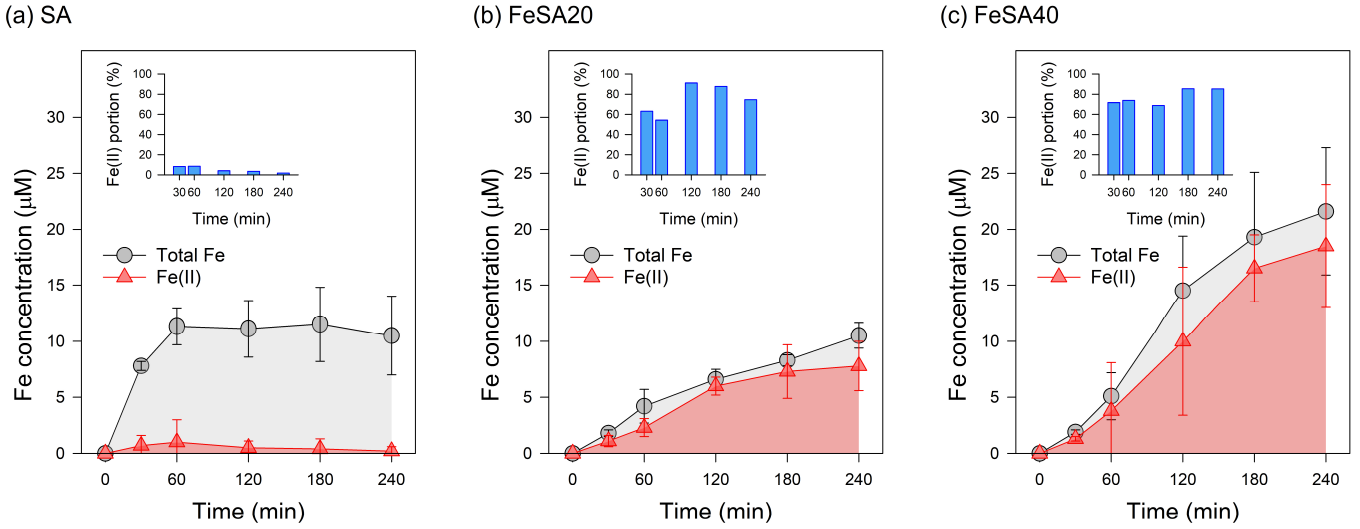

Figure 4. Iron leaching behavior of SA and FeSA at pH 4. Temporal changes in dissolved Fe(II) and total dissolved Fe concentrations in suspensions containing (**a**) SA, (**b**) FeSA20, and (**c**) FeSA40. Insets show the proportion of Fe(II) in total dissolved Fe ([Fe(II)]/[total Fe] × 100). Reaction conditions: Solid concentration = 1 g/L.

More notably, the proportion of Fe(II) in the dissolved Fe pool differed markedly between SA and FeSA. In SA, Fe(II) remained below 1.0 μM (<10% of the total dissolved Fe) throughout the experiment and accounted for only a minor fraction of the dissolved Fe, indicating that Fe was released predominantly as Fe(III) (Figure 4a). In contrast, Fe(II) constituted the majority of dissolved Fe from both FeSA20 and FeSA40 over most of the leaching period. At 240 min, Fe(II) concentrations reached 7.8 ± 2.2 μM for FeSA20 and 18.5 ± 5.5 μM for FeSA40, corresponding to approximately 75% and 85% of the total dissolved Fe, respectively (Figure 4b,c). The predominance of dissolved Fe(II) contrasts with the Fe(III)-dominated surface oxidation state identified by XPS (Figure 2d), indicating that the oxidation state of dissolved Fe does not necessarily reflect that of Fe at the solid surface. This difference may arise from preferential dissolution of reduced Fe species or reduction of Fe(III) before or during dissolution, as suggested by previous studies on the reductive dissolution of Fe(III) oxides [39,40]. For the latter possibility, carbonaceous species surviving thermal treatment may participate in electron transfer to Fe(III). Redox-active oxygen-containing functionalities and aromatic/graphitic carbon structures have been reported to facilitate electron transfer in thermally derived carbonaceous materials [41–43]. In this regard, FTIR and C 1s XPS analyses confirmed potentially relevant carbonaceous features, including aromatic C=C and oxygen-containing C–O and C=O species (Figure 2b,d). However, these characteristics were similar among SA, FeSA20, and FeSA40, with no appreciable differences in either the FTIR band profiles or C 1s binding energies.

To further examine whether Fe conditioning nevertheless altered the reducing capability of the ash, we compared SA, FeSA20, and FeSA40 by monitoring the reduction of Cu(II) to Cu(I), which was stabilized by complexation with DMP (Figure S4). Upon addition of each material to the test solution, the Cu(I) concentration increased rapidly during the initial reaction period and gradually approached a plateau within 60 min. SA, FeSA20, and FeSA40 reduced 67.2 ± 1.5%, 67.4 ± 1.4%, and 73.0 ± 0.2% of the initial Cu(II), respectively, at 60 min, demonstrating comparable reducing capabilities regardless of Fe conditioning. Thus, the predominance of

 https://doi.org/10.53941/ges.2026.100033

Fe(II) released from FeSA cannot be explained simply by differences in the overall reducing capability of the materials. Rather, Fe reduction may depend on Fe-specific interfacial interactions and the mode of Fe association within the ash matrix [39,44,45], which are not fully captured by the Cu(II) reduction assay. In particular, the relatively high concentrations of Cu(II) (1 mM) and DMP (4.8 mM) used in this assay may alter interfacial interactions and electron-transfer processes compared with those occurring during Fe leaching. Further investigation, including the development of reducing-capacity assays that better represent Fe-leaching conditions, is therefore required to elucidate the mechanisms governing the contrasting Fe speciation during leaching.

3.5. Contribution of Dissolved Fe to Fenton Oxidation

To assess whether the micromolar levels of dissolved Fe observed in Figure 4 could make a meaningful contribution to pollutant oxidation, we examined the homogeneous Fenton oxidation of 0.1 mM 4-CP using 5 μM Fe(II) (≈0.28 mg/L), approximately corresponding to the dissolved Fe concentration observed during the early stage of Fe leaching. Unlike the adsorption–oxidation experiments described in Section 3.3, the reaction was initiated directly by the addition of 10 mM H_2O_2 at a constant pH of 4, and the degradation of 4-CP and consumption of H_2O_2 were simultaneously monitored (Figure 5). For comparison, parallel experiments were performed with SA, FeSA20, FeSA40, Fe_2O_3, and α-FeOOH under otherwise identical conditions.

The homogeneous Fe(II) system exhibited substantially faster 4-CP degradation than the solid materials, achieving 61.6% removal within the first 15 min and reaching nearly complete degradation (99.3%) at 240 min (Figure 5a). In comparison, the 4-CP removal efficiencies at 240 min were 21.7 ± 2.7%, 68.3 ± 3.8%, and 78.3 ± 2.3% for SA, FeSA20, and FeSA40, respectively. Among the reference Fe oxides, Fe_2O_3 showed negligible 4-CP removal (3.2 ± 1.1%), whereas α-FeOOH achieved 88.9 ± 15.5% removal. These results demonstrate that even a micromolar concentration of dissolved Fe(II) can drive substantial Fenton oxidation and that the contribution of dissolved Fe should not be considered negligible solely on the basis of its low concentration.

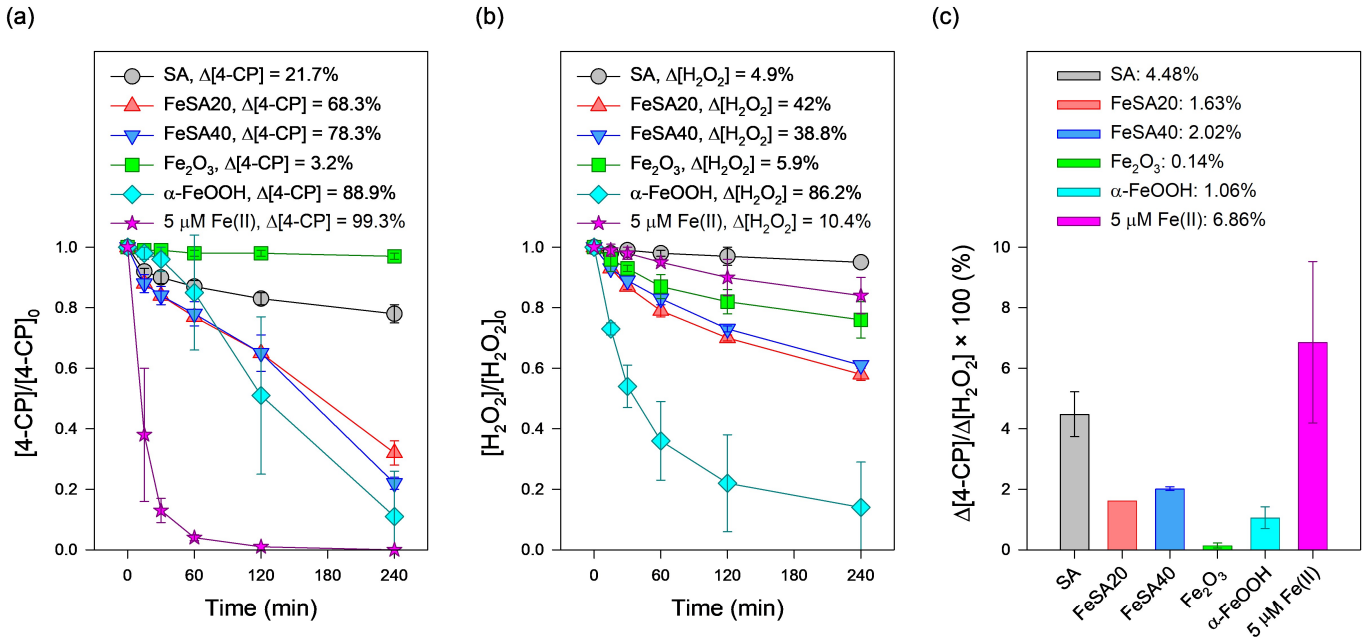

Figure 5. Comparison of Fenton oxidation of 4-CP using SA, FeSA, reference Fe oxides, and dissolved Fe(II) at pH 4. Temporal profiles of (**a**) 4-CP degradation and (**b**) H_2O_2 consumption, and (**c**) stoichiometric efficiencies for H_2O_2 utilization. Experimental conditions: $[4\text{-CP}]_0$ = 0.1 mM, $[H_2O_2]_0$ = 10 mM, and solid concentrations = 1 g/L.

A further distinction was observed in H_2O_2 consumption (Figure 5b). At 240 min, SA consumed only 4.9 ± 0.2% of the initial H_2O_2, whereas FeSA20 and FeSA40 consumed 42.0 ± 2.3% and 38.8 ± 0.1%, respectively. The substantially greater H_2O_2 consumption by FeSA than by SA indicates that Fe incorporated during conditioning actively promoted H_2O_2 decomposition. However, the increased H_2O_2 consumption was not proportionally reflected in 4-CP removal, indicating inefficient utilization of H_2O_2 for pollutant oxidation. This behavior was even more evident for the reference Fe oxides (i.e., Fe_2O_3 and α-FeOOH), which showed substantial H_2O_2 consumption relative to the corresponding 4-CP removal. A previous study similarly reported very low stoichiometric efficiencies (generally <0.2% at pH 5.5–8.5) for pure iron oxide-catalyzed oxidation, defined as Δ[target organic compound]/Δ[H_2O_2] × 100, and suggested non-radical H_2O_2 decomposition and scavenging of surface-generated

•OH by the oxide itself as possible causes [46]. Accordingly, the same metric was applied to the present systems at pH 4 to further evaluate the efficiency of H_2O_2 utilization for 4-CP removal (Figure 5c). The stoichiometric efficiency was highest for the homogeneous Fe(II) system (6.86%), followed by SA (4.48%), FeSA40 (2.02%), FeSA20 (1.63%), α-FeOOH (1.06%), and Fe_2O_3 (0.14%), indicating that H_2O_2 utilization for 4-CP removal was considerably less efficient in the Fe-containing solid systems than in the homogeneous system containing only 5 μM Fe(II).

To further evaluate the contribution of Fe species released from FeSA, a filtrate-transfer experiment was conducted using FeSA40 (Figure S5). FeSA40 was equilibrated in pH-adjusted DI water at pH 4 for 1 h, followed by removal of the solids through a 0.45 μm membrane filter. The recovered filtrate contained 4.20 μM total dissolved Fe, almost entirely as Fe(II) (4.18 μM). Upon addition of 4-CP and H_2O_2, the filtrate achieved 92.0 ± 2.3% 4-CP removal within 60 min, comparable to the homogeneous Fenton system containing 5 μM Fe(II). It should be noted that 4-CP removal proceeded substantially more slowly in the FeSA40 suspension after the 60-min adsorption period (Figures 3a and S5), despite the release of micromolar Fe(II) under similar conditions (3.8 ± 4.3 μM after 60 min at pH 4; Figure 4c). This difference raises the possibility that FeSA solids may adversely affect Fenton oxidation through competing reactions, including nonproductive H_2O_2 consumption or scavenging of reactive oxidants by WAS-derived constituents.

These findings have important implications for interpreting the Fenton activity of Fe-containing WAS-derived materials. The substantial oxidation of 4-CP achieved with micromolar concentrations of dissolved Fe(II) highlights the importance of considering dissolved Fe contributions when evaluating the apparent heterogeneous Fenton activity of Fe-containing solids. Notably, previous studies on Fe-containing WAS-derived materials reported leached Fe concentrations within a similar micromolar range (3.8–11.8 μM at pH 4 [13,15,16,18]), although the oxidation states of the dissolved Fe were not identified. The present results suggest that FeSA can serve not only as an adsorbent but also as a source of catalytically active Fe(II) capable of supporting homogeneous Fenton oxidation in the aqueous phase. Nevertheless, this interpretation cannot be directly extended to other Fe-containing WAS-derived materials because of differences in their preparation methods and experimental conditions. Thus, further systematic investigation is required to distinguish the relative contributions of homogeneous and heterogeneous Fenton pathways among different Fe-containing WAS-derived materials and, accordingly, to reassess their functional roles in Fenton oxidation.

From a practical perspective, it is worth noting that indiscriminately increasing the Fe(III) coagulant dose to enhance the oxidation performance of FeSA is not a justifiable approach. The primary objective of Fe conditioning is to improve WAS dewaterability, whereas the subsequent use of FeSA as an adsorbent or oxidation catalyst represents an additional benefit of sludge treatment. Although FeSA40 exhibited higher oxidation performance toward 4-CP, its preparation required an Fe dose exceeding the optimal range for WAS dewatering (10–20 mM). Such excessive Fe addition may increase chemical costs without providing further benefits for WAS dewatering. Instead, the applicability of FeSA should be evaluated using materials produced under dewatering-optimized conditions, while acknowledging their potentially limited oxidation performance toward certain pollutants. Furthermore, the relatively low H_2O_2 utilization efficiency and the need for acidic reaction conditions represent additional challenges for practical application, warranting further research to improve the catalytic performance of FeSA under more practical water treatment conditions.

4. Conclusions

In this study, we assessed Fe-containing WAS-derived ash as an environmental remediation material for the removal of organic pollutants, with a particular focus on its role as a heterogeneous Fenton catalyst. The major findings and implications are summarized as follows:

(1) FeSA, prepared by mimicking a conventional WAS treatment process (including Fe conditioning, dewatering, drying, and thermal treatment), exhibited a porous and predominantly amorphous matrix containing crystalline quartz, an Fe phosphate phase, and residual carbonaceous components.

(2) Adsorption performance was comparable between SA (without Fe conditioning) and FeSA, whereas FeSA exhibited greater oxidative pollutant removal than SA at pH 4. This oxidative performance decreased drastically at pH 5.

(3) FeSA released dissolved Fe at pH 4, with Fe(II) accounting for the majority of the released Fe, whereas Fe released from SA was predominantly Fe(III). The dissolved Fe concentration generally increased with increasing Fe content in FeSA.

(4) A homogeneous Fenton system containing only 5 μM Fe(II), comparable to the level of Fe(II) released from FeSA, achieved substantially faster degradation of 0.1 mM 4-CP and exhibited the highest stoichiometric efficiency for H_2O_2 utilization (6.86%), compared with 4.48% for SA and ≤2.02% for FeSA and the reference Fe-containing solids.

(5) These findings suggest that FeSA may be more appropriately viewed as a multifunctional material capable of adsorbing pollutants and serving as a reservoir of catalytically active Fe(II) for homogeneous Fenton reactions, rather than as a heterogeneous Fenton catalyst.

 https://doi.org/10.53941/ges.2026.100033

Supplementary Materials

The additional data and information can be downloaded at: https://media.sciltp.com/articles/others/2611201445325611/GES-26080251-SI.pdf. Figure S1. SEM images of the FeSA20 sample. Figure S2. SEM images of the FeSA20 sample at progressively higher magnifications. Figure S3. Point EDS analyses of FeSA20 at three different locations. Figure S4. Temporal changes in Cu(I) concentration during Cu(II) reduction by SA, FeSA20, and FeSA40. Figure S5. Time-dependent 4-CP removal in a homogeneous Fenton system containing 5 μM Fe(II), the FeSA40 filtrate, and the FeSA40 suspension at pH 4.

Author Contributions

Y.H.C.: investigation, data curation, writing—original draft preparation; M.K.: methodology, visualization; C.L.: resources, funding acquisition, writing—reviewing and editing; M.S.K.: conceptualization, supervision, writing—reviewing and editing. All authors have read and agreed to the published version of the manuscript.

Funding

This work was supported by the Ministry of Education of the Republic of Korea and the National Research Foundation of Korea (NRF-RS-2023-00213501).

Institutional Review Board Statement

Not applicable.

Informed Consent Statement

Not applicable.

Data Availability Statement

Data will be made available on request.

Conflicts of Interest

The authors declare no conflict of interest.

Use of AI and AI-Assisted Technologies

During the preparation of this work, the authors used ChatGPT (OpenAI) to improve the language, grammar, clarity, and readability of the manuscript. After using this tool, the authors reviewed and edited the content as needed and take full responsibility for the content of the published article.

References

1. Metcalf & Eddy, Inc.; AECOM. *Wastewater Engineering: Treatment and Resource Recovery*, 5th ed.; McGraw-Hill Education: New York, NY, USA, 2014; pp. 1449–1658.
2. Zhou, K.; Yang, Y.; Liu, B.; et al. Waste to worth: A new approach to treat wastewater sludge. *Sep. Purif. Technol.* **2023**, *305*, 122412.
3. Yuan, H.; Zhu, N. Progress of improving waste activated sludge dewaterability: Influence factors, conditioning technologies and implications and perspectives. *Sci. Total Environ.* **2024**, *912*, 168605.
4. Janiga-MacNelly, A.; Lavado, R. Unveiling the mysteries: A deep dive into extracellular polymeric substances in activated sludge systems of wastewater treatment plants. *Environ. Technol. Rev.* **2024**, *13*, 572–596.
5. Li, Y.; He, P.; Zhang, H.; et al. A critical review of *in-situ* moisture distribution detection and characterization techniques utilizing deep dewatering for organic waste. *J. Environ. Manag.* **2025**, *373*, 123710.
6. Pirouzi, A.; Asrami, M.R.; Sabzehmeidani, M.M. Advancement factors in sludge dewatering technology for wastewater treatment from engineering and economic perspectives: A review. *Environ. Funct. Mater.* **2024**, *3*, 171–186.
7. Chen, Y.; Chio, C.; Boteju, R.; et al. Sludge dewatering: A review of conventional methods and microbial assisted approaches. *J. Environ. Manag.* **2026**, *405*, 129776.
8. Tan, J.; Huang, Y.; Chi, B.; et al. Comparative study of iron and aluminium coagulants in conditioning sludge: Sludge dewatering performance, physicochemical properties, and risk of heavy metal migration. *J. Environ. Chem. Eng.* **2024**, *12*, 113168.
9. Chen, X.X.; Yuan, Y.W.; Gao, Y.Y.; et al. Beyond charge neutralization: Self-skeletization of inorganic coagulants reinforces pore networks for enhanced sludge dewatering. *Water Res.* **2026**, *288*, 124546.
10. Sharma, A.K.; Ghodke, P.K.; Chen, W.H. Progress in green adsorbent technologies from sewage sludge for wastewater remediation and carbon capture: A sustainable approach towards clean environment. *Curr. Opin. Green Sustain. Chem.* **2024**, *46*, 100883.
11. Agoe, A.K.; Poulopoulos, S.G.; Sarbassov, Y.; et al. Investigation of Sewage Sludge–Derived Biochar for Enhanced Pollutant Adsorption: Effect of Particle Size and Alkali Treatment. *Energies* **2024**, *17*, 4554.
12. Pachaiappan, P.; Massa, M.; Riva, L.; et al. Dual valorization of sewage sludge ash through phosphorus recovery and wastewater remediation. *J. Environ. Manag.* **2026**, *404*, 129410.
13. Tu, Y.; Tian, S.; Kong, L.; et al. Co-catalytic effect of sewage sludge-derived char as the support of Fenton-like catalyst. *Chem. Eng. J.* **2012**, *185–186*, 44–51.
14. Gu, L.; Zhu, N.; Zhou, P. Preparation of sludge derived magnetic porous carbon and their application in Fenton-like degradation of 1-diazo-2-naphthol-4-sulfonic acid. *Bioresour. Technol.* **2012**, *118*, 638–642.
15. Gu, L.; Guo, H.; Zhu, N.; et al. Adsorption and Fenton-like degradation of naphthalene dye intermediate on sewage sludge derived porous carbon. *J. Hazard. Mater.* **2013**, *246–247*, 145–153.
16. Mohedano, A.F.; Monsalvo, V.M.; Bedia, J.; et al. Highly stable iron catalysts from sewage sludge for CWPO. *J. Environ. Chem. Eng.* **2014**, *2*, 2359–2364.

17. Ye, G.; Zhou, J.; Huang, R.; et al. Magnetic sludge-based biochar derived from Fenton sludge as an efficient heterogeneous Fenton catalyst for degrading Methylene blue. *J. Environ. Chem. Eng.* **2022**, *10*, 107242.
18. Yuan, S.J.; Dai, X.H. Facile synthesis of sewage sludge-derived mesoporous material as an efficient and stable heterogeneous catalyst for photo-Fenton reaction. *Appl. Catal. B Environ.* **2014**, *154–155*, 252–258.
19. Zhu, Y.; Xie, Q.; Deng, F.; et al. The differences in heterogeneous Fenton catalytic performance and mechanism of various iron minerals and their influencing factors: A review. *Sep. Purif. Technol.* **2023**, *325*, 124702.
20. Wang, N.; Yang, Y.; Wang, K.; et al. A comprehensive review on heterogeneous Fenton-like catalyst for the oxidation degradation of organics in wastewater. *J. Water Process Eng.* **2025**, *72*, 107444.
21. Wang, Y.; Chen, Y.; Wu, D. Iron (Oxyhydr) Oxides in Heterogeneous Fenton Processes: Structure-Activity Relationships in Hydrogen Peroxide Decomposition Pathways. *Catalysts* **2026**, *16*, 169.
22. Tamura, H.; Goto, K.; Yotsuyanagi, T.; et al. Spectrophotometric determination of iron(II) with 1,10-phenanthroline in the presence of large amounts of iron(III). *Talanta* **1974**, *21*, 314–318.
23. Besada, A. Analytical Use of Copper (II)-Neocuproine in The Spectrophotometric Determination of Hydrazines. *Anal. Lett.* **1988**, *21*, 1917–1925.
24. Eisenberg, G. Colorimetric Determination of Hydrogen Peroxide. *Ind. Eng. Chem. Anal. Ed.* **1943**, *15*, 327–328.
25. Minero, C.; Lucchiari, M.; Maurino, V.; et al. A quantitative assessment of the production of •OH and additional oxidants in the dark Fenton reaction: Fenton degradation of aromatic amines. *RSC Adv.* **2013**, *3*, 26443–26450.
26. Kim, M.S.; Kim, H.H.; Lee, K.M.; et al. Oxidation of microcystin-LR by ferrous-tetrapolyphosphate in the presence of oxygen and hydrogen peroxide. *Water Res.* **2017**, *114*, 277–285.
27. Gallard, H.; De Laat, J.; Legube, B. Influence du pH sur la vitesse d'oxydation de composés organiques par Fe^{II}/H_2O_2. Mécanismes réactionnels et modélisation. *New J. Chem.* **1998**, *22*, 263–268.
28. Choi, H.D.; Shin, M.C.; Kim, D.H.; et al. Removal characteristics of reactive black 5 using surfactant-modified activated carbon. *Desalination* **2008**, *223*, 290–298.
29. Pengthamkeerati, P.; Satapanajaru, T.; Singchan, O. Sorption of reactive dye from aqueous solution on biomass fly ash. *J. Hazard. Mater.* **2008**, *153*, 1149–1156.
30. Slater, B.; McCormack, A.; Avdeef, A.; et al. PH-Metric logP.4. Comparison of Partition Coefficients Determined by HPLC and Potentiometric Methods to Literature Values. *J. Pharm. Sci.* **1994**, *83*, 1280–1283.
31. Wojnárovits, L.; Takács, E. Irradiation treatment of azo dye containing wastewater: An overview. *Radiat. Phys. Chem.* **2008**, *77*, 225–244.
32. Buxton, G.V.; Greenstock, C.L.; Helman, W.P.; et al. Critical Review of rate constants for reactions of hydrated electrons, hydrogen atoms and hydroxyl radicals (•OH/•O^-) in Aqueous Solution. *J. Phys. Chem. Ref. Data* **1988**, *17*, 513–886.
33. Chen, Y.; Miller, C.J.; Waite, T.D. Heterogeneous Fenton Chemistry Revisited: Mechanistic Insights from Ferrihydrite-Mediated Oxidation of Formate and Oxalate. *Environ. Sci. Technol.* **2021**, *55*, 14414–14425.
34. Chen, Y.; Miller, C.J.; Waite, T.D. pH Dependence of Hydroxyl Radical, Ferryl, and/or Ferric Peroxo Species Generation in the Heterogeneous Fenton Process. *Environ. Sci. Technol.* **2022**, *56*, 1278–1288.
35. De Laat, J.; Gallard, H. Catalytic Decomposition of Hydrogen Peroxide by Fe(III) in Homogeneous Aqueous Solution: Mechanism and Kinetic Modeling. *Environ. Sci. Technol.* **1999**, *33*, 2726–2732.
36. Clarizia, L.; Russo, D.; Di Somma, I.; et al. Homogeneous photo-Fenton processes at near neutral pH: A review. *Appl. Catal. B Environ.* **2017**, *209*, 358–371.
37. Schwertmann, U.; Schulze, D.G.; Murad, E. Identification of Ferrihydrite in Soils by Dissolution Kinetics, Differential X-ray Diffraction, and Mössbauer Spectroscopy. *Soil Sci. Soc. Am. J.* **1982**, *46*, 869–875.
38. Schwertmann, U. Solubility and dissolution of iron oxides. *Plant Soil* **1991**, *130*, 1–25.
39. Zinder, B.; Furrer, G.; Stumm, W. The coordination chemistry of weathering: II. Dissolution of Fe(III) oxides. *Geochim. Cosmochim. Acta* **1986**, *50*, 1861–1869.
40. Huang, J.; Jones, A.; Waite, T.D.; et al. Fe(II) Redox Chemistry in the Environment. *Chem. Rev.* **2021**, *121*, 8161–8233.
41. Sun, T.; Levin, B.D.A.; Guzman, J.J.L.; et al. Rapid electron transfer by the carbon matrix in natural pyrogenic carbon. *Nat. Commun.* **2017**, *8*, 14873.
42. Feng, D.; Shou, J.; Guo, S.; et al. Co-catalysis of trace dissolved Fe(III) with biochar in hydrogen peroxide activation for enhanced oxidation of pollutants. *RSC Adv.* **2022**, *12*, 17237–17248.
43. Hou, M.; Gu, X.; Fan, Y.; et al. Pyrogenic Carbon Structures Determined Electron Transfer Mechanism Enhancing Iron Autotrophic Denitrification: Role of Oxygen-Containing Functional Groups and Graphitic Structures. *Environ. Sci. Technol.* **2026**, *60*, 19300–19311.
44. Jang, J.H.; Brantley, S.L. Investigation of Wüstite (FeO) Dissolution: Implications for Reductive Dissolution of Ferric Oxides. *Environ. Sci. Technol.* **2009**, *43*, 1086–1090.
45. Aeppli, M.; Voegelin, A.; Gorski, C.A.; et al. Mediated Electrochemical Reduction of Iron (Oxyhydr-)Oxides under Defined Thermodynamic Boundary Conditions. *Environ. Sci. Technol.* **2018**, *52*, 560–570.
46. Pham, A.L.T.; Lee, C.; Doyle, F.M.; et al. A Silica-Supported Iron Oxide Catalyst Capable of Activating Hydrogen Peroxide at Neutral pH Values. *Environ. Sci. Technol.* **2009**, *43*, 8930–8935.